NTNU

Norwegian University of
Science and Technology

Boundary conditions for the lattice Boltzmann method

Mass conserving boundary conditions for moving walls

erwan le coupanec

Master of Science in Engineering and ICT

Submission date: June 2010

Supervisor: Bernhard Müller, EPT

Co-supervisor: Joris Verschaeve, EPT

Norwegian University of Science and Technology
Department of Energy and Process Engineering

Problem Description

Background and objective:

The lattice Boltzmann method is a new numerical method of computational fluid dynamics (CFD). Conventional fluid solvers are based on the Navier-Stokes equations describing fluid motion based on a continuous picture of matter. The lattice Boltzmann method instead relies on discrete particles having an idealized movement on a lattice. Similar to the case of particles with continuous movement, it can be shown that the Navier-Stokes equations can be recovered from the statistical description of these particles. The numerical solution of these lattice Boltzmann equations has computational advantages over conventional solvers based on the Navier-Stokes equations. However, boundary conditions are still an issue for this method, since there is no clear picture what happens with these particles at walls or interface. The master thesis will focus on boundary conditions of the lattice Boltzmann method.

The following questions should be considered in the project work:

1. Implementation of the mass conserving boundary conditions for walls at rest for the lattice Boltzmann method.
2. Analytical derivation of a similar formulation for moving walls.
3. Implementation of this new formulation.
4. Verification of the boundary conditions.

Assignment given: 18. January 2010
Supervisor: Bernhard Müller, EPT

Master thesis 2010: Lattice Boltzmann Bathnagar-Gross-Krook no-slip boundary condition for tangentially moving walls

Erwan LE COUPANEC

June 11, 2010

Master thesis in Engineering fluid dynamics, TEP4925 - Spring semester 2010
Supervisors in numerical fluid dynamics group: Bernhard Müller and Joris Verschaeve

NTNU

Norges Teknisk-naturvitenskapelige Universitet i Trondheim
Department of energy and process engineering

Abstract

Based on the no-slip boundary condition for walls at rest for the lattice Boltzmann Bathnagar-Gross-Krook method by J.C.G. Verschaeve [10], a no-slip boundary condition for walls with a tangential movement is derived. Numerical tests verify that the present boundary condition is second order accurate and stable for relaxation frequencies close to two.

Acknowledgements

I would like to show my gratitude to my supervisors Bernhard Müller and Joris Verschaeve for their guidance, support and encouragement along the realisation of this master project. I am grateful to Joris Verschaeve for his numerous advices at every step of the project and the patient corrections he provided me during the final redaction of this thesis. I would like to thank him and the numerical fluid dynamics group at NTNU for the occasion they gave me to attend a course, at the university of Geneva, about the Palabos [8] library used to do the coding part of the project. Thanks goes to Jonas Lätt, Bastien Chopard, Orestis Malaspinas, Andrea Parmangiani and Daniel Lagrava who organized this course in Geneva, and thus helped me to begin coding using the Palabos library.

Contents

Part I
Introduction

Interest for the lattice Boltzmann method has been growing continuously in the last 20 years [9]. The lattice Boltzmann method is a numerical scheme used to solve the incompressible Navier-Stokes equation. Opposed to standard Navier-Stokes solvers it does not solve the incompressible Navier-Stokes equations directly but instead adopts a 'particle' perspective. The molecular point of view of the method allows to handle complex flows such as multiphase flows, or flows in porous media in a natural way [6].
In the lattice Boltzmann method the flow is described by models for collision between particles. Lattice Boltzmann algorithms consist of two steps. One is a local step, called collision, describing changes of particle density due to collisions at each grid node. The other, so called streaming step, is not local and is responsible for streaming of particles from lattice nodes to others. The particle distribution function is the essential object of the method. Macroscopic quantities, such as density or momentum, are recovered as statistical moments of this particle distribution function.
This thesis focuses on the no-slip boundary condition for walls with a tangential movement. The present derivation is based on the no-slip boundary condition for walls at rest by J.C.G. Verschaeve [10]. The difficulty of boundary conditions in the lattice Boltzmann method is to assign proper values to the particle distributions leaving the boundary into the bulk-fluid. The adopted formulation is responsible for transmitting the wall effect to the fluid. Thus the value of the velocity or the density is taken as an input for the formulation, but further assumptions are necessary, respecting the physics at the boundary. Such a formulation for the no-slip boundary condition at tangentially moving walls is derived here. This formulation is then applied to several benchmark cases in order to evaluate its accuracy and stability.
We start by presenting different aspects of the method in part II p. 7. It is meant to emphasize results from the numerous existing works, subsequently used in the derivation of the boundary condition. A more detailed introduction to the method and developed arguments should be looked for in the works this section refers to. The part III p. 12 presents briefly two boundary conditions we compare the present boundary condition to. In part IV p. 14, the formulation for no-slip boundary condition at tangentially moving walls is derived following the ideas developed in the article of J.C.G. Verschaeve [10]. The part V p. 22 shows the results obtained in the cases of three steady flows, namely Poiseuille flow, half Poiseuille flow, Couette flow, flow in a lid-driven cavity, and the unsteady periodic flow of the second problem of Stokes. The flow in a lid-driven cavity apply the present boundary condition on each of the four walls. An additional simulation has also

been performed to compare the mass variations obtained with the present formulation to the ones obtained with the two formulations presented in part III. Apart from this additional case, the numerical verification focuses on the method's order of accuracy. The present discussion is concluded in part VI p.35.

Part II
Lattice Boltzmann Bathnagar-Gross-Krook

This section presents the main aspect of the lattice Boltzmann method. We treat only the lattice Boltzmann Bathnagar-Gross-Krook version of the lattice Boltzmann method. More details on the lattice Boltzmann Bathnagar-Gross-Krook method can be found in [6, 12]. The LB method considers flows on a particle scale. Therefore we are interested in the particle density distribution depending on space, velocity and time. Similar to the Boltzmann theory of gases for continuous systems, the particle density distribution function gives the probability to find a particle moving with a velocity $\vec{\xi}$ at position $\vec{x}$ and time t. Such a continuous distribution function $f(\vec{x}, t, \vec{\xi})$ is given in [12](p.139). It needs to be underlined that, apart from space and time, this distribution depends on the particle velocity. The macroscopic variables: density ρ, velocity $\vec{u}$ and pressure p usually inside the computations in classical CFD are in the LBM computed using the microscopic variables: the particle distribution function.
The Boltzmann equation gives a basic kinetic model to describe the evolution of the particle distribution function [5]:

$$\frac{\partial f}{\partial t} + \vec{u}.\vec{\nabla} f = J(f). \tag{II.1}$$

where the left hand side represents the free transport of the particles while the right hand side describes their interactions and is called collision operator. This collision operator has to ensure the conservation of the collision invariants: mass, momentum and energy and should allow the system to tend towards a Maxwell-Boltzmann distribution. A broader discussion can be found in [12] (p.143).

A lattice Boltzmann simulation is performed on an equidistant Cartesian grid. The time stepping of the temporal discretization is constant. The discretization of the particle distribution function requires, apart from the spacial and temporal discretization, a discretization of the velocity space. The lattice Boltzmann method resolves this difficulty by resorting to a reduction of the velocity space to a finite set of velocity vectors. These velocity vectors are chosen in such a way that the system is isotropic and that the velocities are interconnecting the grid nodes of the computational domain. Weights are associated to each velocity in order to account for their differences in length [1]. The grid together with the sets of velocities and weights form the lattice. The $D2Q9$ lattice is a common choice for problems in two dimensions. It reduces the two-dimensional velocity space to a set of nine velocities as defined in table II and shown in figure 1. The velocities

i	0	1	2	3	4	5	6	7	8
t_i	4/9	1/36	1/9	1/36	1/9	1/36	1/9	1/36	1/9
$\vec{c_i}$	$(0,0)$	$(-1,1)$	$(-1,0)$	$(-1,-1)$	$(0,-1)$	$(1,-1)$	$(1,0)$	$(1,1)$	$(0,1)$

Table 1: the lattice velocities $\vec{c_i}$ and the lattice weights t_i of the $D2Q9$ lattice

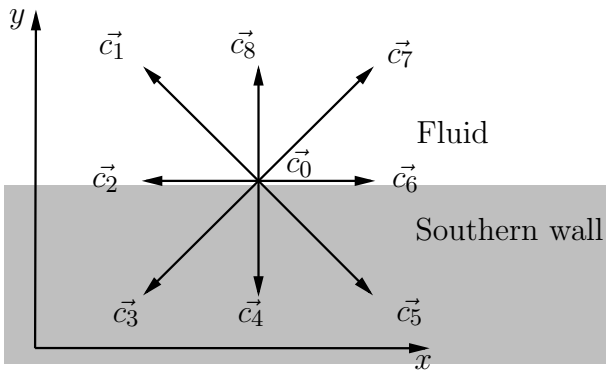

Figure 1: D2Q9 lattice

coordinates are here expressed in lattice units. In the lattice system of units the grid spacing and time steps are usually:

$$\Delta x = \Delta t = 1. \tag{II.2}$$

An implication of the model is that a particle travels the grid step Δx in one time step Δt so that the particle speed or lattice constant c is given by:

$$c = \frac{\Delta x}{\Delta t} = 1. \tag{II.3}$$

The speed of sound c_s, characteristic of lattices, is then often defined as:

$$c_s = \frac{c}{\sqrt{3}}. \tag{II.4}$$

This value is the numerically most stable [6] and therefore commonly adopted.

The physical units are the units of the reference flow. The superscript star is always meant to indicate the use of the physical units. The reference flow is described by the usual set of dimensionless variables and the Reynolds number. Thus the reference velocity U^* and the characteristic length L^* are set to one and the variation of the Reynolds number is achieved by changing the value of the kinematic viscosity ν^*.

For the simulations the characteristic length L^* is divided in a finite number N of intervals. N is the spatial resolution of the simulation. Thus, the space discretization in physical units writes as follows:

$$\delta x = \frac{L^*}{N} = \frac{1}{N}. \tag{II.5}$$

The time stepping in physical units δt is defined relatively to δx as it will be explained in section V.1 p. 22. The lower case δ indicates here the physical units.

Once the lattice defined, the particle distribution function is reduced to a set of population functions, each of the populations f_i describes the particle distribution for one velocity $\vec{c}_i$. Thus for the $D2Q9$ lattice, nine populations describe the behaviour of the ensemble of particles and:

$$f_i(\vec{x}, t) = f(\vec{x}, t, \vec{c}_i). \tag{II.6}$$

In the following all the formulations are given with respect to the $D2Q9$ lattice without loss of generality.

The Boltzmann equation for this set of populations gives a set of equations so called lattice Boltzmann equation [6]:

$$f_i(\vec{x} + \vec{c}_i, t+1) - f_i(\vec{x}, t) = J_i(f_0, ..., f_8)(\vec{x}, t), \text{ i=0,...,8.} \tag{II.7}$$

This equation is split into two steps in the algorithm of the lattice Boltzmann method. The collision step stands for the collisions particles undergo at each node and is a local transformation of the populations. The superscript *in* and *out* indicate populations respectively entering the collision step and going out of the collision step. Hence the collision is written as follows, where the populations are taken at node $\vec{x}$ and time t:

$$f_i^{out} = f_i^{in} + J_i(f_0^{in}, ..., f_8^{in}), \text{ i=0,...,8.} \tag{II.8}$$

The streaming step carries information from each node to its neighbouring nodes. Thus at each node the populations are translated to one of the neighbouring nodes according to the velocity component they are associated with. The superscript *ps* indicates populations which have just been streamed. We have:

$$f_i^{ps}(\vec{x} + \vec{c}_i, t+1) = f_i^{out}(\vec{x}, t) \tag{II.9}$$

On bulk-fluid nodes we have $f_i^{in} = f_i^{ps}$. On the other hand, at boundaries, no population is streamed onto the node corresponding to the velocities pointing out of the wall (indices 1,8 and 7 in figure 1), and therefore a precollision (*in*) value has to be found for these missing populations. Defining appropriate values for the missing populations at the boundary node is precisely the role of the boundary condition formulation.

The lattice Boltzmann Bathnagar-Gross-Krook method is the simplest lattice Boltzmann method and therefore enjoys a big popularity. The collision conserves mass and momentum. The collision operator is expressed as a relaxation of the population f_i towards an equilibrium distribution function f_i^{eq}:

$$J_i = -\omega(f_i - f_i^{eq}). \tag{II.10}$$

The equilibrium distribution function can be seen as a truncated expansion of the Maxwellian distribution [12] [6]. It is defined in the LBGK model by:

$$f_i^{eq} = \rho t_i\big(1 + \frac{1}{c_s^2}\vec{c_i}.\vec{u} + \frac{1}{2c_s^4}\vec{Q_i} : \vec{u} \otimes \vec{u}\big) \tag{II.11a}$$

$$\text{with } \vec{Q_i} = \vec{c_i} \otimes \vec{c_i} - c_s^2\vec{I}, \text{ a second order tensor.} \tag{II.11b}$$

The flow velocity u and the flow density ρ are recovered by computing the statistical moments of the distribution functions as shown thereafter:

$$\rho(\vec{x}, t) = \sum_{i=0}^{8} f_i(\vec{x}, t) \tag{II.12a}$$

$$(\rho\vec{u})(\vec{x}, t) = \sum_{i=0}^{8} \vec{c_i} f_i(\vec{x}, t) \tag{II.12b}$$

The third order statistical moment yields a second order tensor used subsequently:

$$\mathbf{\Pi} = \sum_{i=0}^{8} \vec{c_i}\vec{c_i} f_i. \tag{II.13}$$

The Chapman-Enskog multiscale analysis allows to recover the governing equations for these mascroscopic quantities. The method treats the "physical phenomena occurring at different scales" separately [6]. The populations are expanded with respect to a small parameter ϵ identified with the Knudsen number[1].

$$f_i = f_i^{(0)} + \epsilon f_i^{(1)} + \epsilon^2 f_i^{(2)} + ... \tag{II.14}$$

To reach the governing equations the populations must be expanded around the equilibrium functions, so the zeroth order term of each population is identified with the matching equilibrium distribution function, $f_i^{(0)} = f_i^{eq}$. The rest of first order is called non equilibrium part of the populations and written $f_i - f_i^{eq} = f_i^{neq}$. With these notations, a necessary condition to ensure mass conservation during collision reads:

$$\sum_i f_i^{neq} = 0. \tag{II.15}$$

[1] the Knudsen number is the ratio $\epsilon = \frac{\lambda}{L}$ between the molecules mean free path and the reference length

A necessary condition to ensure momentum conservation during collision reads:

$$\sum_i \vec{c}_i f_i^{neq} = \vec{0}. \tag{II.16}$$

The first order terms of the populations are explicitly given by the Chapman-Enskog multiscale analysis [6]:

$$f_i^{(1)} = -\frac{t_i}{c_s^2 \omega}\left(\mathbf{Q}_i : \rho\nabla\vec{u} - \vec{c}_i\nabla : \rho\vec{u}\vec{u} + \frac{1}{2c_s^2}(\vec{c}_i.\nabla)(\mathbf{Q}_i : \rho\vec{u}\vec{u})\right). \tag{II.17}$$

The multiscale analysis shows that the macroscopic quantities obey the incompressible Navier-Stokes equations for small Mach and Knudsen numbers.

$$\nabla.\vec{u} = \vec{0}, \tag{II.18}$$

$$\partial_t \rho\vec{u} + \nabla.(\rho\vec{u}\vec{u}) = -\nabla p + \nabla.\tau, \tag{II.19}$$

where the pressure is given by the equation of state for an ideal gas,

$$p = c_s^2 \rho. \tag{II.20}$$

The stress tensor τ is defined in terms of the rate of strain tensor $\mathbf{S} = \left(\nabla\vec{u} + (\nabla\vec{u})^T\right)/2$ as,

$$\tau = 2\nu\rho\mathbf{S}. \tag{II.21}$$

The kinematic viscosity is found to be related to the relaxation frequency by:

$$\nu = c_s^2(\frac{1}{\omega} - \frac{1}{2}). \tag{II.22}$$

The rate of strain tensor is expressed in terms of the first order part of the statistical moment $\mathbf{\Pi}^1$:

$$\mathbf{\Pi}^{(1)} = \sum_i \vec{c}_i\vec{c}_i f_i^{(1)} = -\frac{2c_s^2}{\omega}\rho\mathbf{S}. \tag{II.23}$$

When deriving the incompressible Navier-Stokes equations II.18, II.19 as well as equation II.17 from the lattice Boltzmann equations, terms of second order and higher in space, time and Mach number were neglected. Therefore, equations II.18, II.19, II.17 are respected up to the following error composed of three contributions:

$$E = O(\delta x^2) + O(\delta t^2) + O(Ma^2). \tag{II.24}$$

The third contribution scaling like M_a^2 is the compressibility error. In the next sections, if a result contains the error defined in (II.24), it is indicated by the expression "up to second order".

Part III

Some wet boundary conditions for LBGK

With wet boundary conditions the boundary nodes are infinitesimally close to the wall, but still in the fluid. They are opposed to the bounce-back boundary condition that places the wall at half way between the boundary nodes and the first row of fluid nodes. The bounce-back rule sets a zero velocity on the boundary. It needs a grid dependent treatment of the wall position in order to conserve the second-order accuracy of the lattice Boltzmann method. Therefore it won't be used in the simulations of part V. It is important to remark that for wet boundary conditions the collision step is performed on all the lattice, including on boundary nodes, because the boundary nodes are inside the bulk-fluid domain. With the bounce-back boundary condition, this is not the case since the boundary nodes lie outside the fluid. The present boundary condition is a wet boundary condition. It is compared to two other wet boundary conditions in the simulations: the boundary condition of Zou and He and the local regularized boundary condition of Jonas Lätt. The two latter formulations can be applied as inflow and outflow conditions, and do not deteriorate the second order accuracy of the method.

We present briefly here the two wet boundary conditions which the present boudary condition will be compared to. We reduce this presentation to a two-dimensional flow simulated with a $D2Q9$ lattice. Furthermore we only look at the case of a node on a southern wall that we allow to move tangentially ($U_n = 0$). We start by explaining the general problem of boundary conditions for the lattice Boltzmann method.

As explained in the first part (p. 9), we need values for the populations entering the collision step f_i^{in} for i=0,...,8. The available information lies in the set of streamed populations f_i^{ps} for i=1,7,8,0,2,6. Equations (II.12a) and (II.12b) yield the following system taking in account the values of the macroscopic variables on the boundary.

$$\left\{\begin{array}{lcl} \rho & = & \sum_{i=0}^{8} f_i \\ \rho U_t & = & f_7 - f_1 + f_6 - f_2 + f_5 - f_3 \\ \rho \underbrace{U_n}_{0} & = & f_1 - f_3 + f_8 - f_4 + f_7 - f_5 \end{array}\right. \tag{III.1}$$

The populations pointing towards the wall (3,4,5) and the tangential populations (0,2,6) are known after streaming:

$$f_i^{in} = f_i^{ps}, \text{i=3,4,5,0,2,6.} \tag{III.2}$$

The three populations pointing in the bulk-fluid domain (1,7,8) are unknown. The density is also unknown but not the tangential velocity. Thus the system (III.1) has three equations but four unknowns.

1 Boundary condition of Zou and He [13] for a southern tangentially moving wall

The idea of this boundary condition, enunciated by Zou and He in their article in 1997, is to bounce back only the non-equilibrium part of the incoming population normal to the wall, which has the index 4 in our case,

$$f_8^{in} = f_8^{eq} + f_4^{neq}. \tag{III.3}$$

This equation is a closure relation for the system (III.1).
For a Dirichlet inlet condition in velocity the system can be solved similarly except that $U_t = 0$ and $U_n \neq 0$.
With the equation of state (II.20), knowing the density is equivalent to knowing the pressure. Therefore for a Dirichlet outlet condition in pressure the system can be solved, using once again the assumption of bounce back of the non-equilibrium parts of the incoming normal population.

2 Local regularized boundary condition of J. Lätt [6] for a southern tangentially moving wall

The regularization method of Jonas Lätt is developed in his PhD thesis [6] in the chapter four. In this method, the knowledge of ρ, $\vec{u}$ and $\mathbf{S}$ allows to reconstruct the population at each node. The non-equilibrium parts are obtained by the formula:

$$f_i^{neq} \approx -\frac{\rho t_i}{c_s^2 \omega} \mathbf{Q}_i : \mathbf{S} \tag{III.4}$$

Then the populations are reconstructed using $f_i = f_i^{eq} + f_i^{neq}$. For the local regularized boundary condition of Lätt (ref. [6] in chapter 5 and ref. [7]), the non-equilibrium part of every incoming population normal to the wall (3,4,5) is bounced back into the fluid:

$$f_i^{in} = f_i^{eq} + f_j^{neq} \text{for } (i,j) \in (1,3),(8,4),(7,5). \tag{III.5}$$

Then a reconstruction step as presented above is performed.
Similarly to the one from Zou and He, the local regularized boundary condition can be used for Dirichlet inlet and outlet condition in pressure and velocity.

Part IV
LBGK no-slip boundary condition for tangentially moving walls

The no-slip boundary conditions for tangentially moving walls is derived here using the same physical arguments as the ones used by J.C.G. Verschaeve in his article [10] to derive the no-slip boundary condition for walls at rest. This section regularly refers to the fourth part of this latter article and borrows its structure. Thus, it begins by some results for the rate of strain tensor at the no-slip boundary from hydrodynamic consideration. Then implications for the non-equilibrium parts of the populations are detailed. The derivation is performed after these necessary preliminaries .

1 Hydrodynamic implications at the no-slip boundary

We are interested here in the case where the velocity is tangential and constant along a straight wall. The word "constant" means here independent of the x coordinate if the x-axis is set along the wall. The implications of the no-slip boundary are actually the same as they were for non-moving walls. In particular the implications are still true even if the tangential velocity is time dependent (as in the 2nd problem of Stokes).

First we look at the case of a southern wall and we set the x-axis along it. The wall has a tangential velocity, independant of the x coordinate. Thus the no-slip condition yields on the wall:

$$\frac{\partial u}{\partial x} = \frac{\partial v}{\partial x} = 0. \tag{IV.1}$$

The continuity equation for a two dimensional incompressible flow is $\frac{\partial u}{\partial x} + \frac{\partial v}{\partial y} = 0$. Together with (IV.1), it implies:

$$\frac{\partial v}{\partial y} = 0. \tag{IV.2}$$

Thus the rate of strain tensor writes, similarly to the case of walls at rest:

$$\mathbf{S} = \begin{bmatrix} 0 & \frac{\partial_y u_x}{2} \\ \frac{\partial_y u_x}{2} & 0 \end{bmatrix}. \tag{IV.3}$$

At an internal corner(figure 2) [2], we have $\mathbf{S} = \mathbf{0}$, which is the again the same result as in the case of a non-moving wall.

[2] In the present work, no simulation is done for which external corner are needed.

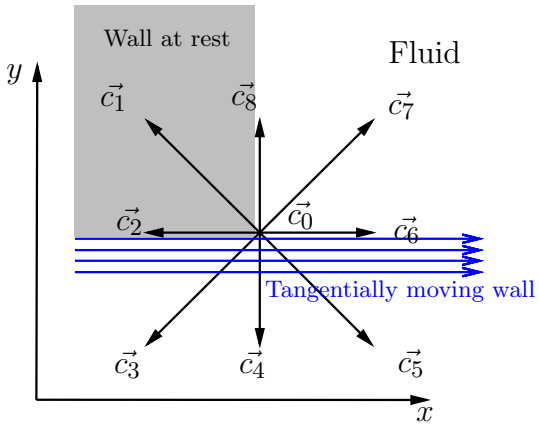

Figure 2: Internal corner with one tangentially moving wall

2 Implications for the leading order term of the non-equilibrium parts

We recall equation II.17 (ref. [6]),

$$f_i^1 = -\frac{t_i}{c_s^2\omega}\left(\mathbf{Q}_i : \rho\nabla\vec{u} - \vec{c}_i\nabla : \rho\vec{u}\vec{u} + \frac{1}{2c_s^2}(\vec{c}_i.\nabla)(\mathbf{Q}_i : \rho\vec{u}\vec{u})\right).$$

We have to compute separately the three terms between parenthesis.

- For the first term, we have from the no-slip equation that:

$$\nabla\vec{u} = \begin{bmatrix} 0 & 1 \\ 0 & 0 \end{bmatrix} \frac{\partial u}{\partial y}.$$

  It follows similarly to the case of walls at rest, since only velocity derivatives play a role here, that:

$$\mathbf{Q}_i : \rho\nabla\vec{u} = 0, \text{ for i=0,2,4,6,8.}$$

$$\mathbf{Q}_i : \rho\nabla\vec{u} = -\frac{\partial u}{\partial y}, \text{ for i=1,5.}$$

$$\mathbf{Q}_i : \rho\nabla\vec{u} = \frac{\partial u}{\partial y}, \text{ for i=3,7.}$$

- For the second term we use (IV.1), (IV.2) and $v = 0$ (tangential ve-

locity):

$$-\vec{c}_i\nabla : \rho\vec{u}\vec{u} = -\rho\Big(c_{ix}(\frac{\partial u^2}{\partial x}+\frac{\partial uv}{\partial y})+c_{iy}(\frac{\partial v^2}{\partial y}+\frac{\partial uv}{\partial x})\Big)$$
$$= -\rho\Big(c_{ix}(2u\underbrace{\frac{\partial u}{\partial x}}_{0}+u\underbrace{\frac{\partial v}{\partial y}}_{0}+\overbrace{v}^{0}\frac{\partial u}{\partial y})+c_{iy}(2\overbrace{v}^{0}\underbrace{\frac{\partial v}{\partial y}}_{0}+u\underbrace{\frac{\partial v}{\partial x}}_{0}+\overbrace{v}^{0}\underbrace{\frac{\partial u}{\partial x}}_{0})\Big)$$
$$= 0$$

- The third term is fully developed thereafter.

$$\vec{c}_i.\nabla\big(\mathbf{Q}_i : \rho\vec{u}\vec{u}\big) = c_{ix}\frac{\partial}{\partial x}\big(\mathbf{Q}_i : \rho\vec{u}\vec{u}\big)+c_{iy}\frac{\partial}{\partial y}\big(\mathbf{Q}_i : \rho\vec{u}\vec{u}\big),$$

and

$$\mathbf{Q}_i : \rho\vec{u}\vec{u} = \rho(Q_{ixx}u^2+2Q_{ixy}uv+Q_{iyy}v^2).$$

Hence we have to derive w.r.t. x (ρ is dropped for convenience),

$$\frac{\partial}{\partial x}\big(Q_{ixx}u^2+2Q_{ixy}uv+Q_{iyy}v^2\big) = 2Q_{ixx}u\underbrace{\frac{\partial u}{\partial x}}_{0}+2Q_{ixy}(\underbrace{\frac{\partial u}{\partial x}}_{0}v+u\underbrace{\frac{\partial v}{\partial x}}_{0})+2Q_{iyy}v\underbrace{\frac{\partial v}{\partial x}}_{0},$$

With (IV.1) and (IV.2), this derivate equals zero. And we still have to derive w.r.t. y,

$$\frac{\partial}{\partial y}\big(Q_{ixx}u^2+2Q_{ixy}uv+Q_{iyy}v^2\big) = 2Q_{ixx}u\frac{\partial u}{\partial y}+2Q_{ixy}(\frac{\partial u}{\partial y}\overbrace{v}^{0}+u\underbrace{\frac{\partial v}{\partial y}}_{0})+2Q_{iyy}\overbrace{v}^{0}\underbrace{\frac{\partial v}{\partial y}}_{0},$$

after have used (IV.1), (IV.2) and $v = 0$, this derivate writes $2Q_{ixx}u\frac{\partial u}{\partial y}$.
Hence,

$$\frac{1}{2c_s^2}\vec{c}_i.\nabla\big(\mathbf{Q}_i : \rho\vec{u}\vec{u}\big) = \frac{\rho}{c_s^2}c_{iy}Q_{ixx}u\frac{\partial u}{\partial y}$$

Finally, we have up to second order:

$$f_i^{neq} = -\rho\frac{t_i}{c_s^4\omega}c_{iy}Q_{ixx}u\frac{\partial u}{\partial y}, \text{i=0,2,4,6,8.} \tag{IV.5}$$

$$f_i^{neq} = -\frac{t_i}{c_s\omega}\frac{\partial u}{\partial y}\big(\frac{\rho}{c_s^2}c_{iy}Q_{ixx}u-1\big), \text{i=1,5.} \tag{IV.6}$$

$$f_i^{neq} = -\frac{t_i}{c_s\omega}\frac{\partial u}{\partial y}\big(\frac{\rho}{c_s^2}c_{iy}Q_{ixx}u+1\big), \text{i=3,7.} \tag{IV.7}$$

We remark that $c_{iy} = 0$ for i=0,2,6 and thus we have the equations:

$$f_i^{neq} = 0, i = 0, 2, 6. \tag{IV.8}$$

These last equations are used to derive the formulation in the following part.

3 Mass conservation

Mass conservation is respected by the collision operator on the bulk-fluid nodes. However, on boundaries, the BGK collision is preceded by the application of the boundary condition and the whole operation has to ensure mass conservation. Thus the mass streamed onto a boundary node from the bulk fluid has to equal the mass streamed out from this boundary node,

$$m^{ps} = m^{out}. \tag{IV.9}$$

The mass streamed in and the mass streamed out can be defined following two different perspectives.

Hollis e.a. [4] adopt a fluid-boundary perspective. According to the fluid-boundary perspective, m^{ps} is the sum of all the populations streamed from nodes of the computational domain, e.g. bulk-fluid and boundary nodes. Similarly m^{out} is the sum of all the populations about to be streamed on the computational domain.

Chopard and Dupuis [2] adopt a fluid perspective whose condition will be used in the derivation of the present boundary condition. m^{ps} is the sum of all populations streamed from bulk-fluid nodes only. Similarly m^{out} is the sum of all the populations about to be streamed to bulk-fluid nodes only. On a straight southern wall, it gives,

$$\begin{aligned} m^{ps} &= f_3^{ps} + f_4^{ps} + f_5^{ps}, \\ m^{out} &= f_1^{out} + f_8^{out} + f_7^{out}, \end{aligned}$$

and on a south west internal corner with one wall moving tangentially (figure 2),

$$\begin{aligned} m^{ps} &= f_3^{ps}, \\ m^{out} &= f_7^{out}. \end{aligned}$$

4 Derivation

We begin by deriving the conditions for a straight southern wall moving tangentially (figure 1) and we establish the conditions for an internal corner (figure 2) at the end of the section.

4.1 Straight southern wall with tangential velocity

We seek values for the populations f_i^{in} after the streaming step. We have the populations f_3^{ps}, f_4^{ps}, f_5^{ps} streamed from bulk-fluid nodes and the populations f_0^{ps}, f_2^{ps}, f_6^{ps} streamed from boundary nodes. The wall velocity $\vec{u}_{wall}$ is known but not the wall density ρ_{wall}. We recall that we can write $f_i^{in} = f_i^{eq} + f_i^{neq}$. Then the constraints for the non-equilibrium parts of the

populations f_i^{neq} are listed as done in ref. [10] p.7. They consist of the collision invariance of mass (II.15), the collision invariance of momentum (II.16) and the expression for the rate of strain tensor (II.23) where f_i^1 have been replaced by f_i^{neq}. Since the rate of strain tensor S keeps the same writing as for walls at rest, the system remains identical:

$$f_1^{neq} + f_2^{neq} + f_3^{neq} = 0 \tag{IV.12a}$$
$$f_5^{neq} + f_6^{neq} + f_7^{neq} = 0 \tag{IV.12b}$$
$$f_1^{neq} + f_8^{neq} + f_7^{neq} = 0 \tag{IV.12c}$$
$$f_3^{neq} + f_4^{neq} + f_5^{neq} = 0 \tag{IV.12d}$$
$$f_0^{neq} + f_2^{neq} + f_6^{neq} = 0 \tag{IV.12e}$$
$$f_2^{neq} - f_4^{neq} + f_6^{neq} - f_8^{neq} = 0 \tag{IV.12f}$$
$$-f_1^{neq} + f_3^{neq} - f_5^{neq} + f_7^{neq} = -\frac{2c_s^2\rho}{\omega} S_{xy} \tag{IV.12g}$$

The equation (IV.12g) is removed from the system for the reason given in ref. [10], which is that the off-diagonal component of the rate of strain tensor is usually an unknown for a straight wall. Again similarly to what is done in ref. [10], the populations coming from bulk-fluid nodes are kept,

$$f_i^{in} = f_i^{ps} \text{ for i=3,4,5,} \tag{IV.13}$$

but not the populations coming from the wall. From this point we have therefore a system of six equations but seven unknowns. The mass conservation according to the perspective of Chopard and Dupuis allows to define the density at the wall.
At the boundary nodes the equilibrium part of the population has the following form:

$$f_i^{eq} = t_i \rho_{wall} \left[1 + \frac{c_{ix} u_x}{c_s^2} + \frac{1}{2c_s^4}(c_{ix}^2 - c_s^2) u_x^2 \right], \tag{IV.14}$$

We have taken here $\vec{U}_{wall} = (u_x, 0)$ where we can have for example $u_x = u(t)$ or $u_x = constant$.
Using equation (IV.12c) the outgoing mass writes:

$$\begin{aligned} m^{out} &= f_1^{out} + f_8^{out} + f_7^{out}, \\ &= (1-\omega)(f_1^{neq} + f_8^{neq} + f_7^{neq}) + f_1^{eq} + f_8^{eq} + f_7^{eq} \\ &= f_1^{eq} + f_8^{eq} + f_7^{eq}, \end{aligned} \tag{IV.15}$$

and the mass conservation condition (IV.9) yields:

$$m^{ps} = f_3^{ps} + f_4^{ps} + f_5^{ps} \tag{IV.16}$$
$$= m^{out}$$
$$= f_1^{out} + f_8^{out} + f_7^{out}, \tag{IV.17}$$

We compute the summation (IV.16) with the help of the expression (IV.14) and replacing the weights t_i and the sound speed c_s^2 by their actual value for the $D2Q9$ lattice,

$$\begin{aligned} m^{ps} &= f_3^{ps} + f_4^{ps} + f_5^{ps}, \\ &= \rho_{wall}\left[\frac{1}{6} + \underbrace{\frac{9}{36}u_x^2 - \frac{3}{12}u_x^2}_{0}\right], \\ &= \frac{1}{6}\rho_{wall}. \end{aligned} \tag{IV.18}$$

We remark that the underlined expression is zero for all value of the tangential velocity. Thus we obtain a definition for the density at the wall similar to the one found by J.C.G. Verschaeve in his article [10]:

$$\rho_{wall} = 6m^{ps}. \tag{IV.19}$$

Using again expression (IV.14) and the identity (IV.13), we have,

$$\begin{aligned} f_3^{eq} + f_4^{eq} + f_5^{eq} =& 6\rho_{wall}, \\ =& f_3^{ps} + f_4^{ps} + f_5^{ps}, \\ =& f_3^{in} + f_4^{in} + f_5^{in}. \end{aligned}$$

Hence equation (IV.12d) is respected by mass conservation.
As done in ref. [10], it could be equally shown here that equations (IV.12c) and (IV.12d) actually lead to the mass conservation in the fluid perspective. Since the condition (IV.12d) is fulfilled by the definition (IV.19) for the wall density, it can be removed from the system and the set of remaining constraints is similar to the one in ref. [10]:

$$\begin{aligned} f_1^{neq} + f_2^{neq} &= -f_3^{neq}, \\ f_6^{neq} + f_7^{neq} &= -f_5^{neq}, \\ f_1^{neq} + f_8^{neq} + f_7^{neq} &= 0, \\ f_0^{neq} + f_2^{neq} + f_6^{neq} &= 0, \\ f_2^{neq} + f_6^{neq} - f_8^{neq} &= f_4^{neq}. \end{aligned}$$

There are now five equations for six unknowns f_i^{neq} for i=0,1,2,6,7,8. We use one of the three closures proposed in ref. [10] to solve the system. This closure is called "no-slip B" in the referenced article and is the one making use of the hydrodynamic implications presented p. 16. For this closure, f_2^{neq} and f_6^{neq} are taken as inputs and set to the values suggested by the equation (IV.8), $f_2^{neq} = f_6^{neq} = 0$. Hence the solutions for the remaining

populations write:

$$
\begin{aligned}
f_1^{neq} &= \frac{1}{2} f_4^{neq} + \frac{1}{2}(f_5^{neq} - f_3^{neq}),\\
f_7^{neq} &= \frac{1}{2} f_4^{neq} - \frac{1}{2}(f_5^{neq} - f_3^{neq}),\\
f_8^{neq} &= -f_4^{neq},\\
f_0^{neq} &= 0.
\end{aligned}
$$

4.2 Internal corner

We treat here the case of an internal corner at the intersection of a wall at rest and a tangentially moving wall (see figure 2. This problem is actually over-defined and a choice has to be made in the implementation with regard to the discontinuity of the velocity at the intersection. First we derive the boundary condition without precising a value for u_x, then we discuss the possible choices. The off-diagonal component of the rate of strain tensor is known, $S_{xy} = 0$, and we have to take in account equations (IV.12a)-(IV.12g). The only population coming from bulk-fluid nodes is f_3 as we can see on figure 2. Hence the mass conservation relation of Chopard and Dupuis reads:

$$
\begin{aligned}
m^{ps} &= f_3^{ps},\\
&= m^{out},\\
&= f_7^{out},\\
&= (1-\omega) f_7^{neq} + f_7^{eq},\\
&= (1-\omega) f_7^{neq} + t_7 \rho_{wall} \left[1 + \frac{u_x}{c_s^2} + \frac{1-c_s^2}{2c_s^4} u_x^2 \right],\\
&= (1-\omega) f_7^{neq} + \frac{1}{36} \rho_{wall} \left[1 + 3u_x + 3u_x^2 \right].
\end{aligned}
$$

We set $f_7^{neq} = 0$ as suggested by the hydrodynamic implications in equation (IV.7). This yields a definition for the corner density:

$$
\rho_{wall} = 36 m^{ps} \left[1 + 3u_x + 3u_x^2 \right]^{-1}. \tag{IV.24}
$$

The populations 1 and 5 do not play a role, therefore we take $f_1^{neq} = f_5^{neq} = 0$. It then follows

$$
f_i^{neq} = 0 \text{ for i=0,...,8.} \tag{IV.25}
$$

The bulk-fluid sees only the population f_7^{out} because all the other populations are either streamed on the boundary (f_i^{out}, i=0,6,8) or simply erased (f_i^{out}, i=1,2,3,4,5). We have whatever the value chosen for u_x,

$$
f_7^{out} = f_7^{eq} = f_3^{ps}, \tag{IV.26}
$$

therefore it is concluded that the choice of the value of the corner velocity has no influence on the bulk-fluid. However a choice is made in the implementation taking $u_x = 0$. This choice can be seen in the results part V.

Part V
Numerical verification

The numerical verification consists of five benchmark cases with increasing complexity. The code used is called *Palabos*. It is developed in *C++* by Jonas Lätt, Orestis Malapinas and other contributors at the university of Geneva and the Ecole Polytechnique Fédérale de Lausanne. This code can be downloaded from their website dedicated to the lattice Boltzmann method [8]. The present boundary condition is implemented creating two new *C++* class, one containing the dynamics of the boundary condition and an other responsible for the instantiation of the boundary condition. The implementation thus uses a similar structure to the implementation of the other boundary conditions available in *Palabos*.

1 Numerical errors and setting of some parameters

An important requirement of the present boundary condition is to not deteriorate the second order accuracy of the method. Thus in the four benchmark cases, Poiseuille flow, half Poiseuille flow, Couette flow and second problem of Stokes, the l_2 norm of the difference between the numerical solution and the theoretical solution is computed for different resolutions N:

$$\epsilon(N) = \frac{\delta x}{\delta t}\sqrt{\frac{\sum_{(i,j)\in I} \|\vec{u}_{num} - \frac{\delta t}{\delta x}\vec{u}^*_{theo}\|^2}{N_I}}. \tag{V.1}$$

The letter I denotes the set formed by all the grid points, which cardinal number is N_I. Inside the square root the units are the lattice ones [3], therefore the error is unscaled by the reference lattice velocity $u_{lattice} = \frac{\delta x}{\delta t}$ [6]. For the verification of the numerical solution for the second problem of Stokes, the previous error is computed several times per temporal period and the average value of each sample is taken.

As seen in the first part p. 11, the error of the method has three contributions. Since we are only considering incompressible flow here, the compressibility component of the error is controlled in all the simulations by setting, as suggested in ref. [5]:

$$\delta t = \delta x^2, \tag{V.2}$$

Hence the total error scales like δx^2. It implies that the lattice viscosity equals the viscosity in physical units, i.e. that the relaxation frequency ω,

[3] u^*_{theo} is in physical units but converted to lattice units by the factor $\frac{\delta t}{\delta x}$

defined in relation (II.22), is independent of the grid refinement.
Successive refinement of the grid leads to a set of values $\epsilon(N)$ for the numerical error. The numerical error can be written with respect to the resolution N as:

$$\epsilon(N) \leq C\delta x^k, \tag{V.3}$$

where C and k are constant independent of N. k is the order of convergence the method.

Except for the second problem of Stokes the chosen benchmark cases are steady flows. Therefore a precise numerical condition of the steady state has to be defined. In the simulations of Poiseuille flow, Couette flow and flow in a lid-driven square cavity, evolution of the velocity field between two consecutive time steps is measured using again the l_2 norm of a difference:

$$\Delta = \frac{\delta x}{\delta t}\sqrt{\frac{\sum_{(i,j)\in I} \|\vec{u}_{new} - \vec{U_{old}}\|^2}{N_I}}. \tag{V.4}$$

Numerical steady state is reached as soon as $\Delta < tol$, with a threshold tol being about 10^{-14}.

2 Poiseuille flow

As a first basic test for the present boundary condition, a Poiseuille flow in two-dimensional channel was simulated. When applied on boundaries with zero velocity, the present boundary condition is exactly the same as the one derived by J.C.G. Verschaeve in his article [10], therefore we wanted to recover similar results to the ones he found (ref. [10], Poiseuille flow, p. 11). The x-axis of the coordinate system is set along the channel walls and the y-axis along the inlet. The reference velocity of the flow is the maximum velocity U^*_{max} reached along the longitudinal axis of symmetry of the channel. The reference length L^* is the width of the channel. We set both variables to 1 and therefore the theoretical solution reads in physical units:

$$u^*_x = 4y^*(1 - y^*), \tag{V.5a}$$
$$u^*_y = 0. \tag{V.5b}$$

The flow pressure is linearly decreasing along the channel with gradient:

$$\nabla p^* = -8\nu. \tag{V.6}$$

The Reynolds number writes:

$$Re = \frac{1}{\nu} = \frac{1}{c_s^2}\frac{1}{\frac{1}{\omega} - \frac{1}{2}}. \tag{V.7}$$

At the inlet and at the outlet a Poiseuille velocity profile (V.5a) is set, using the formulation of Zou and He [13]. Thus the flow is driven by the boundary conditions of the inlet and outlet in this simulation. As initial condition, we impose $\vec{u} = \vec{0}$, and a linearly decreasing pressure along the channel using the value of the gradient (V.6). To impose these values we insert them in the equilibrium parts and set $f_i = f_i^{eq}$ at all the nodes of the bulk-fluid domain. At $\omega = \frac{10}{11}$ (so $Re = 5$), we performed series of simulations with values of the resolution going from $N = 60$ to $N = 190$. Three series were performed in order to compare the present boundary condition with the formulation of Zou and He and the local regularized formulation of Jonas Lätt. The three resulting series of errors $\epsilon(N)$ computed with the formula (V.1) are plotted against the resolution in figure 3. All the bound-

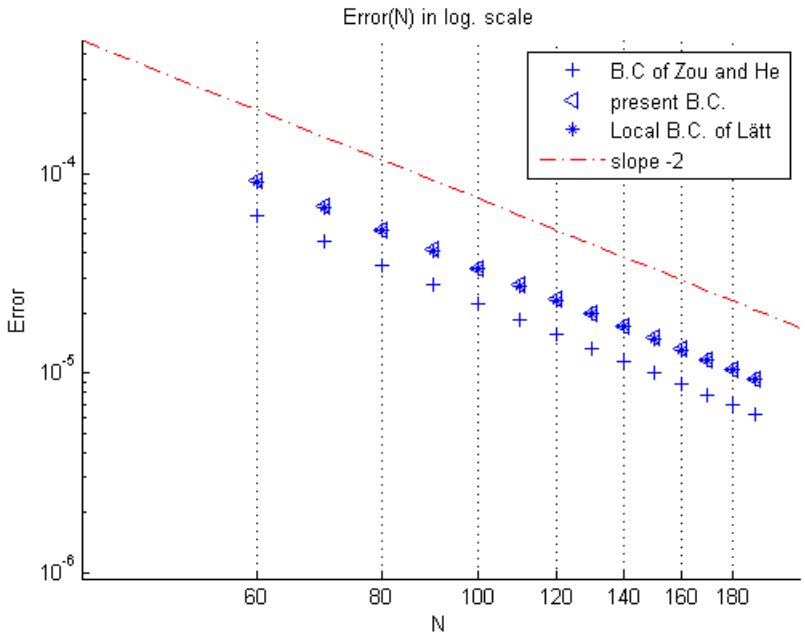

Figure 3: Error scaling of the velocity field for different boundary conditions for Poiseuille flow at $\omega = \frac{10}{11}$.

ary conditions conserve the second-order accuracy of the lattice Boltzmann method. The values for the present boundary condition are very close to the ones for the local boundary condition of Jonas Lätt, whereas the boundary condition of Zou and He give slightly smaller values. Thus the constant C for this last condition is inferior to the constant for the other boundary conditions. Thus, applying the present boundary condition for the Poiseuille flow, we recovered the results presented in [10]. Regarding stability, similar results to [10] were also found. At $N = 60$, the simulation with the bound-

ary condition of Zou and He became unstable at $\omega \approx 1.76$ ($Re = 44$). The simulation with the present boundary condition became equally unstable at $\omega \approx 1.76$ if the boundary condition of Zou and He was used on the inlet and outlet. On the other hand, if the regularized local boundary condition of Lätt was used on the inlet and outlet, the simulation with the present boundary condition stayed stable until $\omega \approx 1.99$ (1.993).

3 Half Poiseuille flow

We verified, with a half Poiseuille flow, the ability of the present boundary condition to transmit a tangential non-zero velocity to the fluid. This flow is the southern half part of a Poiseuille flow of width 2. Thus the width of the domain of the problem is here 1. The reference velocity is equally set to 1 and is reached on the northern boundary of the domain. The coordinate system is set similarly to the way it was in the previous section. The theoretical solution reads in physical units:

$$u_x^* = y^*(2 - y^*), \tag{V.8a}$$

$$u_y^* = 0. \tag{V.8b}$$

The gradient is different from the one we had in the previous section for the Poiseuille flow since the total width of the channel has doubled,

$$\nabla p^* = -2\nu, \tag{V.9}$$

The Reynolds number with respect to the full Poiseuille flow is doubled,

$$Re = \frac{2}{\nu} = \frac{2}{c_s^2} \frac{1}{\frac{1}{\omega} - \frac{1}{2}}. \tag{V.10}$$

On the inlet and outlet, the profile (V.8a) is set similarly to the way it was in the previous section e.g. with the formulation of Zou and He for velocity boundary conditions. As initial condition, we impose $\vec{u} = \vec{0}$ and a linearly decreasing pressure along the y-axis using the value of the gradient (V.9). At $\omega = \frac{10}{11}$ (so $Re = 5$), we performed a series of simulations ($60 < N < 190$) for each of the three boundary conditions (B.C. of Zou and He, local regularized B.C. and the present B.C.). The three resulting series of errors $\epsilon(N)$ computed with the formula (V.1) are plotted against the resolution in figure 4.

This figure shows that the present boundary condition is second-order accurate, similarly to the boundary condition of Zou and He and the local regularized boundary condition of J. Lätt. The constant C is slightly smaller for the boundary condition of Zou and He. Regarding stability, at $N = 60$, the simulation using only the boundary condition of Zou and He became unstable at $\omega \approx 1.76$, while the one using the present boundary condition on the walls and the local regularized boundary condition on the inlet and outlet stayed stable until $\omega \approx 1.99$ (1.992).

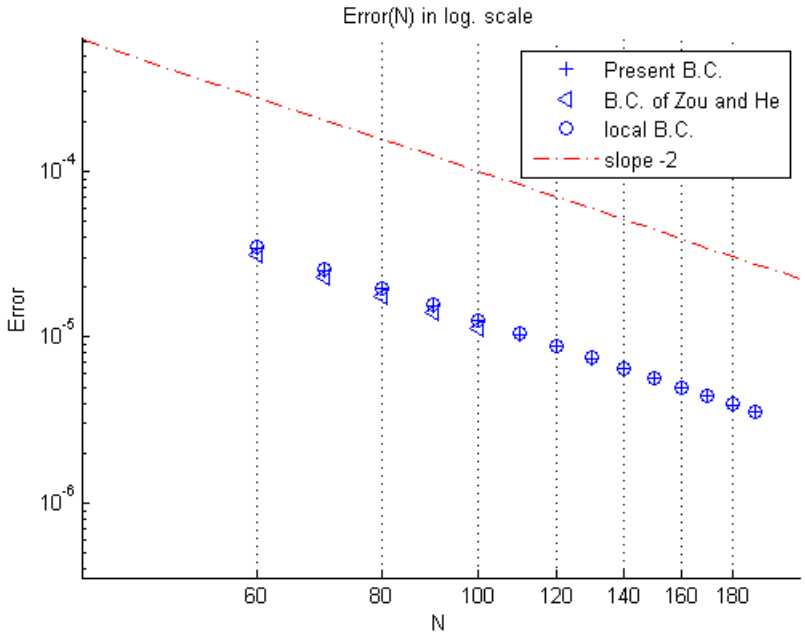

Figure 4: Error scaling of the velocity field for different boundary conditions for half Poiseuille flow at $\omega = \frac{10}{11}$.

4 Couette flow

The Couette flow is a second verification of the ability of the present boundary condition to transmit a non-zero velocity to the fluid. For this problem, the geometry and the coordinate system are the same as for the Poiseuille flow. The maximum velocity $U^* = 1$ is set on the northern boundary. The theoretical velocity is a simple linear profile:

$$u_x^* = y^*, \tag{V.11a}$$
$$u_y^* = 0. \tag{V.11b}$$

The pressure is constant along the channel. The Reynolds number is the same as for the Poiseuille flow.

Opposed to the two previous cases, we set here a periodic streaming between the inlet and outlet. A periodic streaming is performed by connecting the inlet and outlet nodes in a circular manner. For example, the populations on the outlet nodes pointing out of the fluid are streamed onto the inlet nodes. Thus no boundary condition is applied on the inlet and outlet and the flow undergoes only the influence of the boundary condition of the two walls. A constant density $\rho = 1$ and a zero velocity are applied all over the channel as initial condition. The linear Couette profile was actually

solved with a precision close to machine accuracy in all the simulations we performed with the three boundary conditions. The machine accuracy was reached independently of the resolution, thus resulting in an error of the order of magnitude 10^{-14} for all resolution (tested from $N = 3$ to $N = 120$).

5 Flow of the second problem of Stokes [11]

The foregoing benchmark tests certified the second-order accuracy of the present boundary condition for steady flow. In this section we certified the accuracy of the present boundary condition for an unsteady flow simulation with an unsteady tangentially moving wall. The second problem of Stokes can be readily implemented and compared to its analytical solution and therefore has been chosen.

The solution of the second problem of Stokes is an unsteady time-periodic flow. The flow is aligned with the channel walls (x axis) and only a function of the normal (y axis) and time, such that the convective terms become zero. The southern wall oscillates tangentially with a frequency ϕ^*,

$$U^*_{wall}(t) = \cos(\phi^* t^*). \tag{V.12}$$

The analytical velocity profile for this flow writes as follows [11],

$$u^*(t^*, y^*) = \exp\left(-\sqrt{\frac{\phi^*}{2\nu}} y^*\right) \cos\left(\phi^* t^* - \sqrt{\frac{\phi^*}{2\nu}} y^*\right). \tag{V.13}$$

The pressure is constant along the channel. The Reynolds number is $Re = \frac{1}{\nu}$.

The inlet and outlet boundary are connected by a periodic streaming whereas. The initial condition is a constant density $\rho = 1$ and a zero velocity over the whole bulk-fluid domain. At $\omega = \frac{10}{11}$, and for a wall oscillation frequency of value $\phi^* = \frac{2\Pi}{0.2} = 31.416$, the error $\epsilon(N)$ obtained with the present boundary condition is plotted against the resolution N ($N = 60$ to $N = 190$) in figure 5. The results obtained with the boundary condition of Zou and He are plotted as reference. The present boundary condition conserves the second order accuracy of the method similarly to the boundary condition of Zou and He. We notice that the constant C obtained with the present boundary condition has a slightly smaller value than the one obtained with the boundary condition of Zou and He.

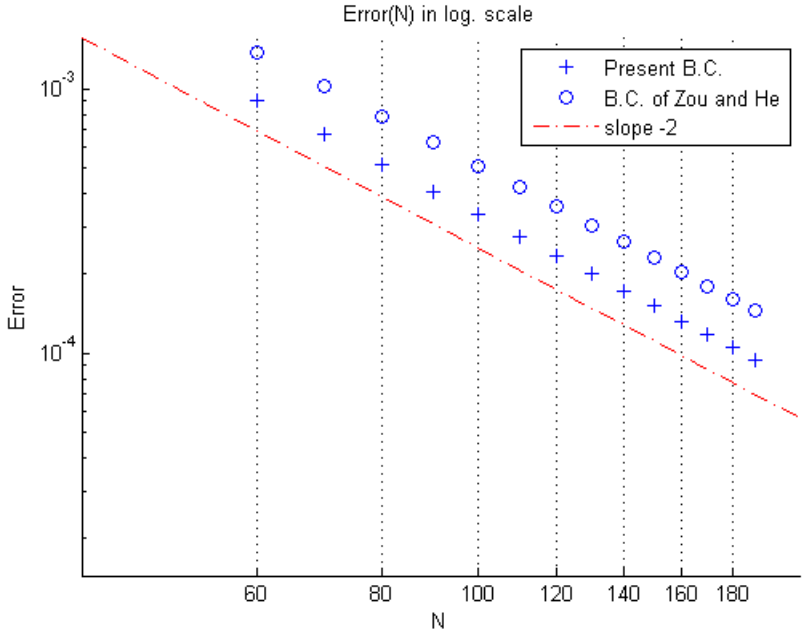

Figure 5: Error scaling of the velocity field for different boundary conditions for the flow solution of the 2nd problem of Stokes at $\omega = \frac{10}{11}$.

6 Flow in a lid-driven square cavity

With the previous benchmark cases we verified that the present boundary condition is able to transmit the effect of a wall with tangential velocity, either constant or periodic. Nevertheless a more complex test case is necessary. Thus, we consider here the laminar flow in a lid-driven cavity. In addition it allows to test the formulation for the internal corners derived in the last section of part IV.

We consider a square cavity which top-wall (x axis) is moving tangentially while the three others are at rest (see figure 6. The length of the cavity edge is $L^* = 1$ and the top-wall velocity is $U^* = 1$. As initial conditions, we impose a zero velocity and a constant density $\rho = 1$ over the whole lattice in every simulation. The results of the simulations performed are compared with the accurate results presented by Ghia e.a. in their article [3]. The results from Ghia e.a. we use here were obtained at a Reynolds number of 100 on a uniform grid of resolution $N = 128$. The profile of the velocity x-component U, along the vertical line through the center of the cavity, and the velocity y-component V, along the horizontal line through the center of the cavity, are provided in their article [3] p.398-399. We performed a simulation at a Reynolds number of 100 ($\omega \approx 1.89$) with a resolution of

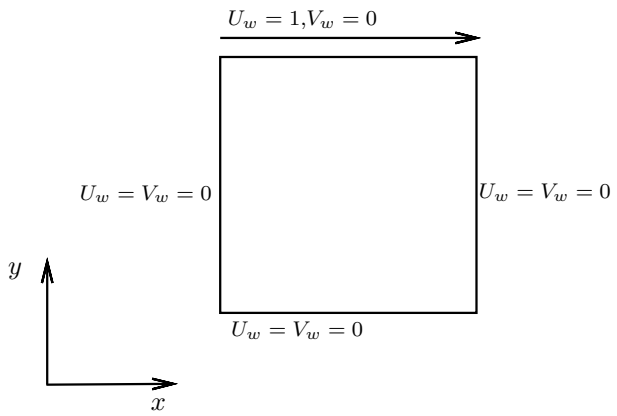

Figure 6: lid-driven square cavity of section V.7 with a step in the density field at $t = 0$

$N = 128$ and applying the present boundary condition on the four walls, including the four internal corners.

Using formula (V.1), an error with respect to the set of values for the x and y components of the velocity from Ghia e.a. is computed. For the present boundary condition, the error obtained is $\epsilon_U = 2.531 \cdot 10^{-3}$ for the U component, and $\epsilon_V = 2.415 \cdot 10^{-3}$ for the V component. On figure 7 p. 30, we plotted the sets of values of the two components of the velocity from the article of Ghia e.a. and the velocity profiles obtained in our simulation. Based on the values of the two errors ϵ_U, ϵ_V, it can be concluded that the problem is solved with satisfying accuracy.

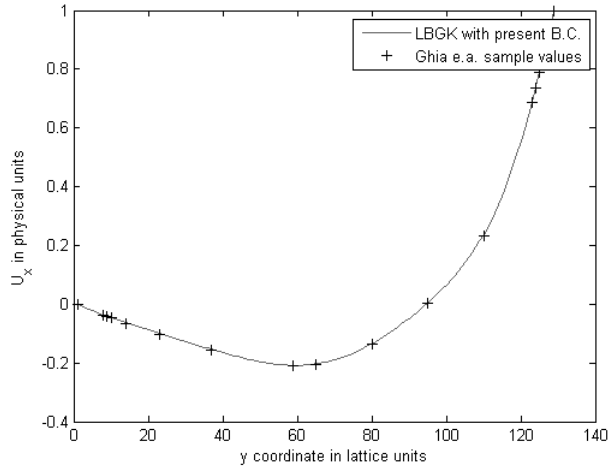

(a) x component (U) along vertical line through geometric center of cavity

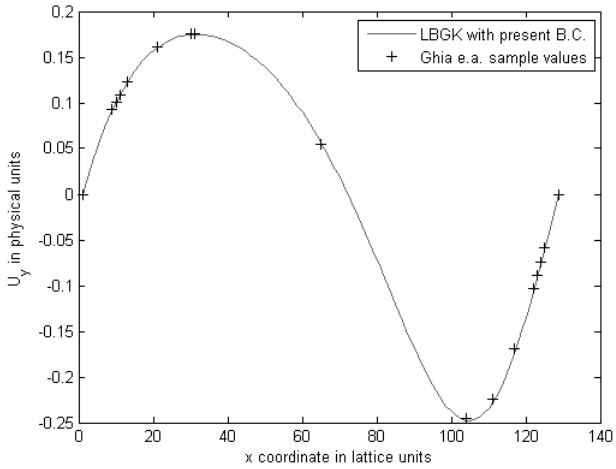

(b) y component (V) along horizontal line through geometric center of cavity

Figure 7: Profiles of the velocity components. For each component, the solid line is a linear interpolation of the values we obtained with the present boundary condition.

As a second graphical verification, figure 12 and 13 in appendix A shows the streamline pattern of the present numerical solution. The pattern we obtained agrees well with the one presented by Ghia e.a. in their article(ref. [3] p.400). To investigate the order of accuracy, we take as reference solution a simulation with a resolution of $N = 256$ and the present boundary con-

dition. We then plot the errors between the velocity field of this reference solution and the velocity field obtained at $N = 16, 32, 64$ and 128 with again the present boundary condition (see figure 8). The graph exhibits a behaviour different from the previous cases since the order of convergence is rather 1 than 2. The flow in the lid-driven cavity poses the problem of

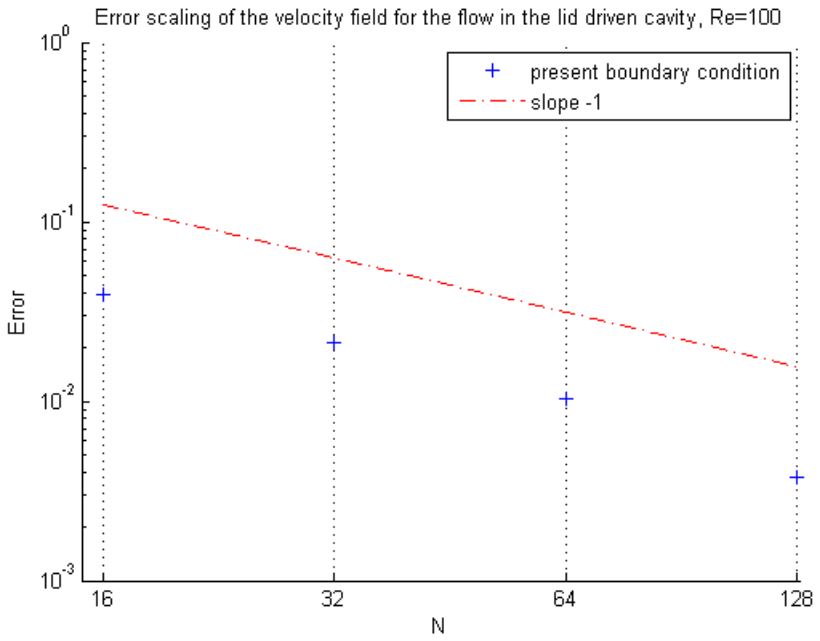

Figure 8: Error scaling of the velocity field for the present boundary condition for the flow in a lid driven cavity at $\omega = 1.89$.

velocity discontinuity in the upper corners, which was described in part IV. This difficulty is not solved properly here and yields spurious oscillations of the pressure value in the two upper corners (see figure 9). The problem of discontinuity at the upper corners leads to similar spurious oscillations with the regularized local formulation of J. Lätt (see figure 10). To verify if the spurious oscillations were responsible for the deterioration of the order of accuracy of the method stated in figure 8, we performed a second check of the order of convergence but only on the half southern part of the cavity (domain $[0, 1] \times [0, 0.5]$). This second check of the order of convergence showed results similar to the first one, namely an order close to 1, only the constant C was slightly inferior to the one obtained in first place. Nevertheless the entire flow in the cavity could be influenced by the velocity discontinuity of the corners, thus the spurious oscillations in the upper corners may still be the cause of the deterioration of the order of accuracy the method.

The pressure field obtained with the present boundary condition, on a domain excluding the upper corners, is plotted on figure 14 in appendix B

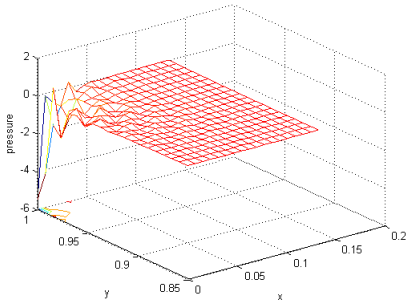

(a) pressure field at upper left corner

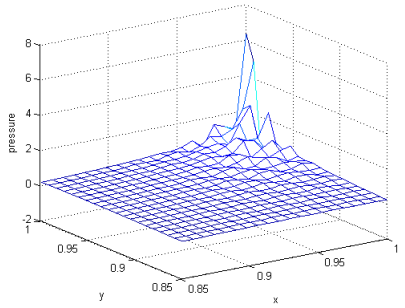

(b) pressure field at upper right corner

Figure 9: Spurious oscillations at the upper corners of the flow in a lid driven cavity. Simulation with $N = 128$ at $Re = 100$ using present corner formulation.

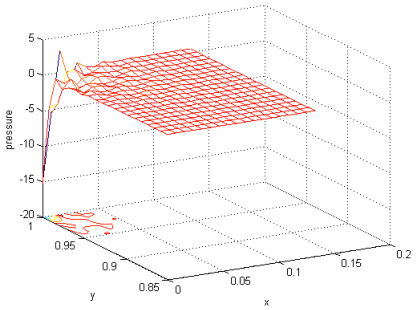

(a) pressure field at upper left corner

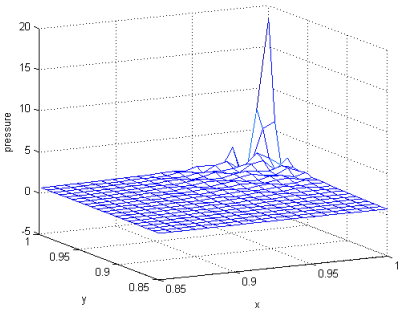

(b) pressure field at upper right corner

Figure 10: Spurious oscillations at the upper corners of the flow in a lid driven cavity. Simulation with $N = 128$ at $Re = 100$ using local regularized formulation for corners of J.Lätt.

p. 38. The velocity field obtained with the present boundary condition is plotted in figure 15 in the same appendix section.

7 Variations of the total mass for the flow in a lid driven square cavity

It was seen, in part IV, that the present boundary condition ensures mass conservation on the boundary nodes from the perspective of Chopard and Dupuis [2]. Thus, this final test case is a numerical investigation of the mass conservation of the present boundary condition.

We consider again the lid-driven cavity of figure 6. The initial conditions are set similarly to the previous section, namely zero velocity and a density of 1 all over the lattice. The resolution is defined to the value $N = 128$, but the value of the relaxation frequency is now $\omega = \frac{10}{11}$ ($Re = 5$).

For the local boundary condition of J. Lätt and the boundary condition of Zou and He, the same treatment is actually applied on the inner corners, e.g. the local regularized formulation for inner corners of Lätt. Thus, these two boundary conditions differ from each other on the straight walls as seen in III. On the other hand the present boundary condition uses the formulation derived in part IV for the inner corners.

In order to take in account the different treatment at the boundaries, the mass on the boundary nodes are counted differently for the different boundary condition. For the local boundary condition of Lätt and the one of Zou and He, the tangential populations and the populations coming from bulk fluid nodes are added out. On a southern wall, it means,

$$m = f_0 + f_2 + f_6 + f_3 + f_4 + f_5, \tag{V.14}$$

while on an internal south/west corner,

$$m = f_3 + f_0 + f_2 + f_4. \tag{V.15}$$

For the present boundary condition, the perspective of Chopard and Dupuis is adopted and therefore the tangential populations are non longer counted. On a southern wall, it means,

$$m = f_3 + f_4 + f_5, \tag{V.16}$$

while on an internal south/west corner,

$$m = f_3. \tag{V.17}$$

The variations with respect to the initial total mass are plotted in figure 7. The variations are unscaled by the initial total mass. The series are plotted from their second term because the scale on both axis is logarithmic and the first couple of each series is $(t = 0, \Delta m = 0)$.

Once at steady state, the variation of the total mass from its initial value is of the order 10^{-14} for the present boundary condition, whereas for the two others the mass variation is of the order 10^{-5}. The graph is plotted

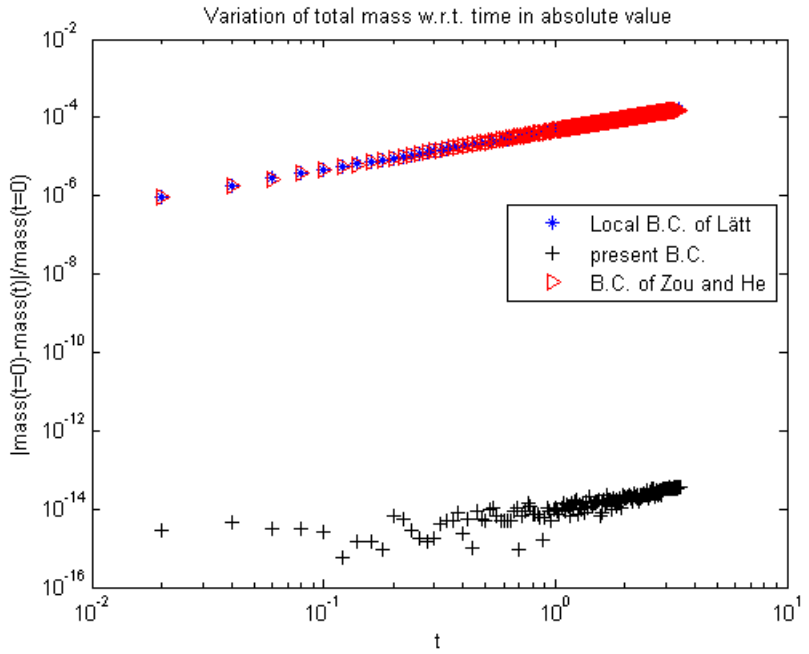

Figure 11: Variations of total mass for different boundary conditions in the case of a square cavity with a step in the density field as initial condition

in logarithmic scale, therefore we can only see the absolute value of the mass variation. However we can precise the sign of the variations. For the present boundary condition the variation oscillates around zero at the beginning but finally takes a negative value at steady state which indicates a loss of mass. For the two other boundary conditions, the signed variation is under zero from the beginning. Thus, we state a loss of mass for the three boundary conditions. However, as expected, the loss of mass is of several orders lower for the present boundary condition than for the two others.

Part VI
Conclusion

We derived a boundary condition for tangentially moving walls for the lattice Boltzmann Bathnagar-Gross-Krook method with $D2Q9$ lattice, based on the no-slip boundary condition for walls at rest derived by J.C.G. Verschaeve in his article [10]. We performed simulations of several steady flow and one time-periodic flow and showed that the present boundary condition did not deteriorate the second-order accuracy of the lattice Boltzmann method. We illustrated, with the test presented in section V.7, the fact used in the derivation IV that the present boundary condition conserves mass from the perspective of Chopard and Dupuis [2]. Further work has to focus on the derivation of a similar boundary condition for three-dimensional problems. The present boundary condition was derived assuming that the velocity component normal to the boundary is zero. Thus, future research has to study the more general case of a moving boundary with a non-zero value for both velocity components.

Part VII
Appendix

A Streamline pattern for the flow in a lid driven cavity

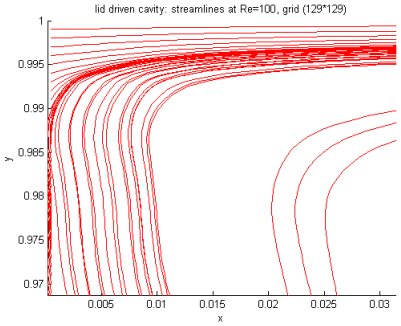

(a) Streamline pattern on the upper left corner

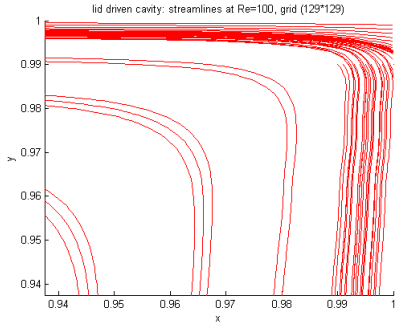

(b) Streamline pattern on the upper right corner

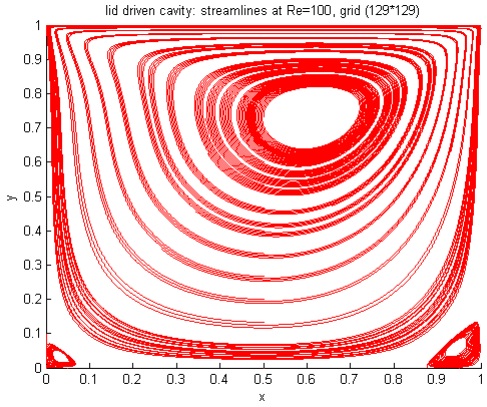

(c) Streamline pattern on the whole domain

Figure 12: Streamlines in the case of the flow in a lid-driven cavity at $Re = 100$, $N = 128$ - present boundary condition

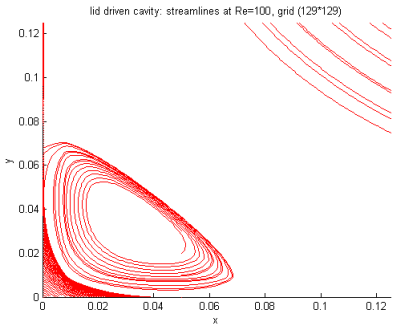

(a) Streamline pattern on the lower left corner

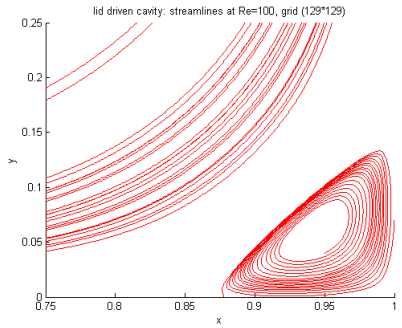

(b) Streamline pattern on the lower right corner

Figure 13: Streamlines in the case of the lid-driven cavity at $Re = 100$, $N = 128$ - present boundary condition

B Pressure field and velocity field for the flow in a lid driven cavity

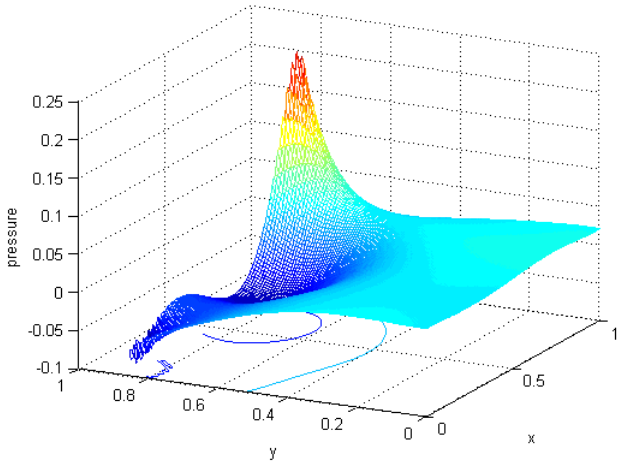

Figure 14: Partial pressure field of the flow in a lid driven cavity obtained with $N = 128$ at $Re = 100$ with the present boundary condition. The plot is restricted to $0 < y < 0.8$ and is thus excluding the upper corners because of the large differences of amplitude between the natural variations of the pressure field and the spurious oscillations at the upper corners.

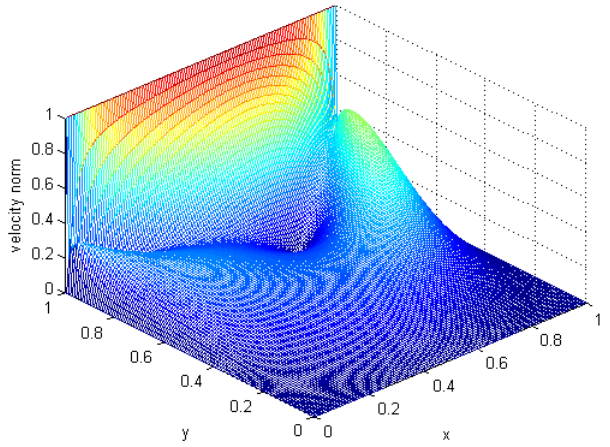

Figure 15: Velocity field of the flow in a lid driven cavity obtained with $N = 128$ at $Re = 100$ with the present boundary condition.

References

[1] H. Chen, I. Goldhirsh, and S.A. Orszag. Discrete rotational symmetry, moment isotropy, and higher order lattice boltzmann models. *J. Sc. Comput.*, 34(1):87–112, 2008.

[2] B. Chopard and A. Dupuis. *Int. J. Mod. Phys. B17*, 103, 2003.

[3] U. Ghia, K.N. Ghia, and C.T. Shin. High-re solutions for incompressible flow using the navier-stokes equations and a multigrid method. *J. Comput. Phys.*, 48:387–411, 1982.

[4] A.P. Hollis, I. Halliday, and C.M. Care. Enhanced, mass-conserving closure scheme for lattice boltzmann equation hydrodynamics. *J.Phys. A 39*, 10589, 2006.

[5] M. Junk. A finite difference interpretation of the lattice boltzmann method. *preprint*, 2001.

[6] J. Lätt. *Hydrodynamic Limit of Lattice Boltzmann Equations*. PhD thesis, Faculté des sciences de l'Université de Genève, 2007.

[7] J. Lätt, B. Chopard, O. Malaspinas, M. Deville, and A. Michler. Straight velocity boundaries in the lattice boltzmann method. *Phys. Rev. E*, 77:056703, 2008.

[8] Malaspinas Orestis Lätt, Jonas. Palabos website. http://www.lbmethod.org/palabos/.

[9] M.C. Sukop and D.T. Thorne. *Lattice Boltzmann Modeling: An Introduction for Geoscientists and Engineers*. Springer, 2006.

[10] J.C.G. Verschaeve. Analysis of the lbgk no-slip boundary condition: Ways to improve accuracy and stability. *Phys. rev.*, 80,036703, 2009.

[11] F.M. White. *Viscous fluid flow*. McGraw-Hill International Edition, 2006.

[12] D.A. Wolf-Gladrow. *Lattice-Gas Cellular Automata and Lattice Boltzmann Models*. Springer, 2000.

[13] Q. Zou and X. He. On pressure and velocity boundary conditions for the lattice boltzmann bgk model. *J. of Stat. Phys.*, 87, 1997.